Patient specific hemodynamic modeling of the aortic root

Ali Hasan
Boyce Griffith

March 28, 2017

Abstract

Patient specific computational models of aortic valve and root dynamics are useful tools for the development of precise treatment schemes. Each year thousands of people worldwide undergo procedures relating to diseased valves. Applying such technology in resource constrained areas to improve the quality of care is a moral imperative for researchers in the field to construct a smaller care differential in global health care quality. However, model construction is a difficult process due to a combination of unstructured input data and heterogeneous computation environments. In this work, we develop a patient specific aortic root model while considering applications for testing medical devices. We further describe a novel method for model construction. We discuss the process of development and implementation of these models as well as the results of the computations.

1 Model Construction

Patient specific computational models promise effective risk mitigation in medical settings in multiple ways from predicting possible ailments to planning surgical procedures. An important part of the process is constructing a specific model for the patient based on patient data. Highly unstructured data acquired from mediums such as electronic medical records or medical imaging are necessary for proper model construction. The lack of structure in the data, however, lends a difficult problem for its analysis and integration into patient care. For such models to be viable, automated means of model construction must be examined.

1.1   Introduction

Medical images from computed tomography (CT) or magnetic resonance (MR) modalities are often used for organ and tissue imaging. This input data in the form of voxels is highly unstructured and is difficult to analyze as a consequence. Patient specific models require the analysis and extraction of relevant data from medical images and are therefore difficult to construct. Segmentation, one particularly difficult process, is discussed in greater detail here.

Segmenting relevant structures from patient image data is a tedious process that typically requires the use of a skilled professional for proper results. Variability in data quality makes segmentation error prone and variable among skilled professionals. Semi-automated and automated methods exist and will be discussed later. Recent advances in computing led to the success of machine learning methods for computer vision tasks such as object segmentation. These methods typically require a wealth of data for proper algorithm training. However, due to the difficulty of data acquisition, few free, open data sets of segmented medical images exists, making such algorithms difficult to construct. Further, the nature of the high dimensional voxel data makes machine learning, particularly convolutional neural networks, extremely expensive for segmentation. Structures such as the aortic root are particularly difficult because of its variability amongst patients, requiring a wealth of data when used with ordinary techniques. We propose a method to circumvent these issues to allow for invariant segmentation of aortic roots with a global shape prior. First, we review the relevant object segmentation methods.

1.2   Background

Development of automatic and semi automatic methods for image segmentation is a current research topic, and many solutions exist. We divide the review of algorithms into level set PDE based models and statistical shape models.

1.2.1   Level set methods

Active contour models were introduced by Kass et al. as a method for object segmentation based on variational calculus [1] where an underlying energy functional is minimized. The functional is of the form:

$$E[u] = \int_C E_{\text{internal}}(u) + E_{\text{image}}(u) + E_{\text{constraint}}(u)\text{ds} \qquad (1)$$

where the internal energies defined by the contour's geometry, image energies defined by the image, and constraint energies are defined by external constraints [1].The

evolution of the curve is defined by:

$$\frac{\partial}{\partial t}C(t, u) = \mathbb{F}\mathbf{n} \tag{2}$$

where $\mathbf{n}$ is the vector normal to C and $\mathbb{F}$ is any acting force on the curve. This formulation makes it particularly suitable for evaluation using the level set method and finite differences [2]. However, active contour models, in the general case, suffer from a lack of convexity, require initialization of seed points, and can provide trivial segmentations with faulty parameter settings. Since no prior information is generally incorporated, the method suffers also with occluded structures or corrupt data. To circumvent this issue, model based priors have been introduced [3].

1.2.2 Model based methods

Model based segmentation methods introduce a shape prior to aid in reinforcing global structure when data may be corrupt [4]. Examples include active shape models introduced by Cootes et al. where a training set of data is used as a basis for shape deformation [5]. A proposal for a probabilistic description of shapes using the cartesian product of intervals spatially distributed is described in [3] as a convex method of image segmentation using shape priors. The energy functional to be minimized is proven to be convex. The issue with many model based methods is the requirement of initial registration of the model with the underlying data, which can be a cumbersome task as well.

1.2.3 Deep learning methods

The decrease in computation cost combined with the influx of data recently increased the popularity of neural network based segmentation techniques. Fully connected convolutional neural networks attain the best results on many object segmentation data sets [6]. However, these techniques have been largely limited to two dimensional approaches because of the computational complexity of 3 dimensional data and require orders of magnitude larger training sets than available in the medical imaging community. In one approach using CNNs on volumetric data, prostates are segmented using a large number of training data [7]. The approach replaces conventional cross entropy loss functions with a Dice coefficient based loss function to circumvent the issues arising with a multinomial logistic loss function.

The mentioned methods require strong initial parameterization and fitting to the image data, and an autonomous system should require no human intervention. We take the beneficial portions of each system to construct a hybrid approach that does not suffer the inconsistencies mentioned in each method.

1.3 Synthetic data generation

Accurate synthetic data is essential for robust model assessment and model training. We propose a method similar to the appearance flow method [8] where a deformation field is sampled from the registration of a series of images with respect to a model. Issues arising with using purely idealized model based methods involve the lack of accurate deformations when training other systems using synthetic data.

1.3.1 Background work

Data synthesis is an important part of medical imaging for validation of analysis models to circumventing the difficulties surrounding annotating new data. Recently, [9] proposed a method of transforming magnetic resonance (MR) imaging to attain the clarity of computed tomography (CT) imaging. The approach uses a generative adversarial network architecture [10] which is trained by training a discriminator to determine generated images from ground truth images. Monte Carlo simulation is used by [11] to sample a distribution of deformed kidney images to construct new images.

1.4 Methods

We base our initial approach on the methods described by Long et al [6] where the methods for semantic segmentation using fully connected nets is described. Our training method uses synthetic images generated from our atlas of structures. We start with the VGG16 [12] object classification network and transform the network into a fully connected network, mapping inputs to outputs of the same dimension. The VGG16 network has many variations of pretrained architectures and the effects of different network architectures are discussed by Simonyan and Zisserman [12] making it a suitable choice for experimentation. Previous attempts suggest the efficacy of learned features from this network [6] though more thought should be given to choosing the underlying model. Furthermore, pre-trained parameters for this network readily exist to easily instantiate the network without the necessary expensive training. However, a pretrained network also looks for other structures in the original ImageNet [13] challenge and may confuse the network. Therefore, we examine segmentation using both learned weights from ImageNet and randomly assigned weights.

Table 1: VGG16 encoding architecture [12]

3x3 filter 64 depth
3x3 filter 64 depth
maxpool
3x3 filter 128 depth
3x3 filter 128 depth
maxpool
3x3 filter 256 depth
3x3 filter 256 depth
3x3 filter 256 depth
maxpool
3x3 filter 512 depth
3x3 filter 512 depth
3x3 filter 512 depth
maxpool
3x3 filter 512 depth
3x3 filter 512 depth
3x3 filter 512 depth
maxpool
fully connected 4096 depth
fully connected 4096 depth
fully connected 1000 depth
softmax

Table 2: FCN8 decoding architecture [6]

1x1 filter 21 depth
2x bilinear upsampling (deconv)
2x bilinear upsampling (deconv)
2x bilinear upsampling (deconv)
1x1 filter

1.4.1   Network Description

The VGG16 network is used as an encoder for our images with output dimension of to produce logits after the softmax layer in the same fashion as Long et al [6]. Each convolution layer consists of a 3x3 filter followed by the application of a nonlinear function, the rectified linear unit (ReLU). Table 1 describes the entire encoding architecture barring the ReLU after each convolution layer. The decoding process uses deconvolutional layers (also known as transpose convolutions) to upsample the output of the encoder with the aim of representing the distilled information from the encoder in the domain of the original image.

All training and evaluation is done on a 2013 Macbook Pro with a 2.6 GHz Intel Core i5 CPU. Unfortunately, TensorFlow does not have GPU bindings for the accompanying Intel HD Graphics 4000 integrated graphics processor. This slightly limits the size capabilities for our network, but provides discussion on the efficacy of using such a system in resource constrained environments. Let $(x_i, y_i) \in T$ where T is our training set, x_i is the input image, and y_i is the true segmentation. For our method, we segment into only foreground and background classes, but the network can be extended to multiple classes as demonstrated in [14].

The images are encoded as one-hot vectors for use with our loss function. We use the cross entropy loss function [14] for updating weight values defined here:

$$H(p, q) = H(p) + D_{KL}(p||q) \tag{3}$$

where

$$D_{KL} = \sum_i p_i \log \frac{p_i}{q_i} \tag{4}$$

$$H(p) = -\sum_i p_i \log p_i \tag{5}$$

is the Kullback-Leiber divergence used for measuring the difference between probability distributions and $H(p)$ is the Shannon entropy of p [15]. Then, this becomes:

$$H(p, q) = -\frac{1}{|I|} \sum_{i \in I} p_i \log q_i \tag{6}$$

where p_i is the predicted pixel value and q_i is the true pixel value and i indexes pixels in an image I. We normalize by the size of the image.

1. Construct set of training images based on regularized geometries.

2. Continue training VGG16 network from initialized learned parameters.

3. Test segmentation abilities on validation set.

4. Determine efficacy using F_1 score and average precision.

5. Generate new training set to further improve performance.

Figure 1: VGG16 network with initialized weights workflow.

1. Construct set of training images based on regularized geometries.

2. Continue training VGG16 network from randomly assigned parameters.

3. Test segmentation abilities on validation set.

4. Determine efficacy using F_1 score and average precision.

5. Generate new training set to further improve performance.

Figure 2: VGG16 network with randomly assigned weights workflow.

1.4.2 Exploiting learned structure from ImageNet

Our method attempts to exploit learned features by further updating weights of our decoder with segmentations developed from an atlas of anatomical structures. Examples of such masks are demonstrated in fig. 3. We begin with only 2 dimensional experimentations. Models can be expanded to 3 dimensions, though previously trained models do not exist as of writing.

1.4.3 Randomly initialized network

Using the architecture described previously, we see how performance changes with convolution filters that do not incorporate knowledge learned from the ImageNet dataset. The network weights are randomly initialized. We again begin with 2 dimensional experimentations using our generated data.

1.4.4 Training

We generate all training sets using analytical descriptions of our geometry. The two shapes we consider are a cross section of the aortic root model and a regular
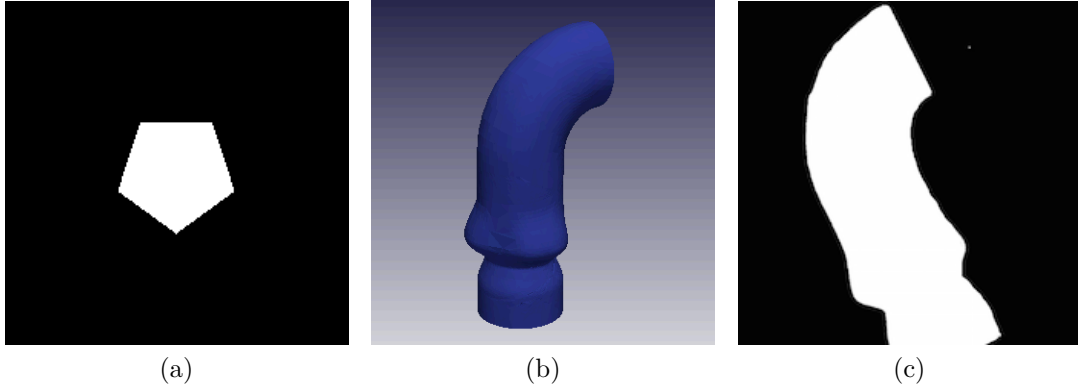
7

Figure 3: Atlas masks for training. Panel (a) shows an example convex polygon geometry, panel (b) shows the 3 dimensional idealized aortic root atlas image, and panel (c) shows a 2 dimensional projection of the aortic root used in our experiments.

pentagon. The pentagon is rotated 25 times for a total training and validation set of 25. Noise and blurring are applied to the training and validation images. The aortic root is rotated 12 times for a total of training and validation set of 12. Fig. 4 shows examples of the distorted images and the ground truth segmentations. Our training set can easily be expanded because of the generative nature of our data.

The network is trained using Adaptive Moment Estimation (Adam) optimizer algorithm which is a gradient descent based optimization algorithm which computes adaptive learning rates for parameters [16]. The learning rate used is 1e-5 with weight decay of 5e-4.

All technology is implemented using TensorFlow [17] using the TensorVision framework, an open source computer vision pipeline [14].

1.5   Results

We test the network on a variety of training schemes and testing images as shown in Fig 5. F1 scores and precision for each validation batch are consistently above 95 for both training shapes. Further, rotations not part of the training set were accurately segmented. It should be noted that the validation images are very idealized and performance on more difficult data should be considered. The segmentations perform very similarly for both networks after similar training periods. For initial training, the pretrained network seems to find structure in the noise. The evolution of the randomly initialized network behaves similarly to an active contour method. Finally, we assess its efficacy on real data.
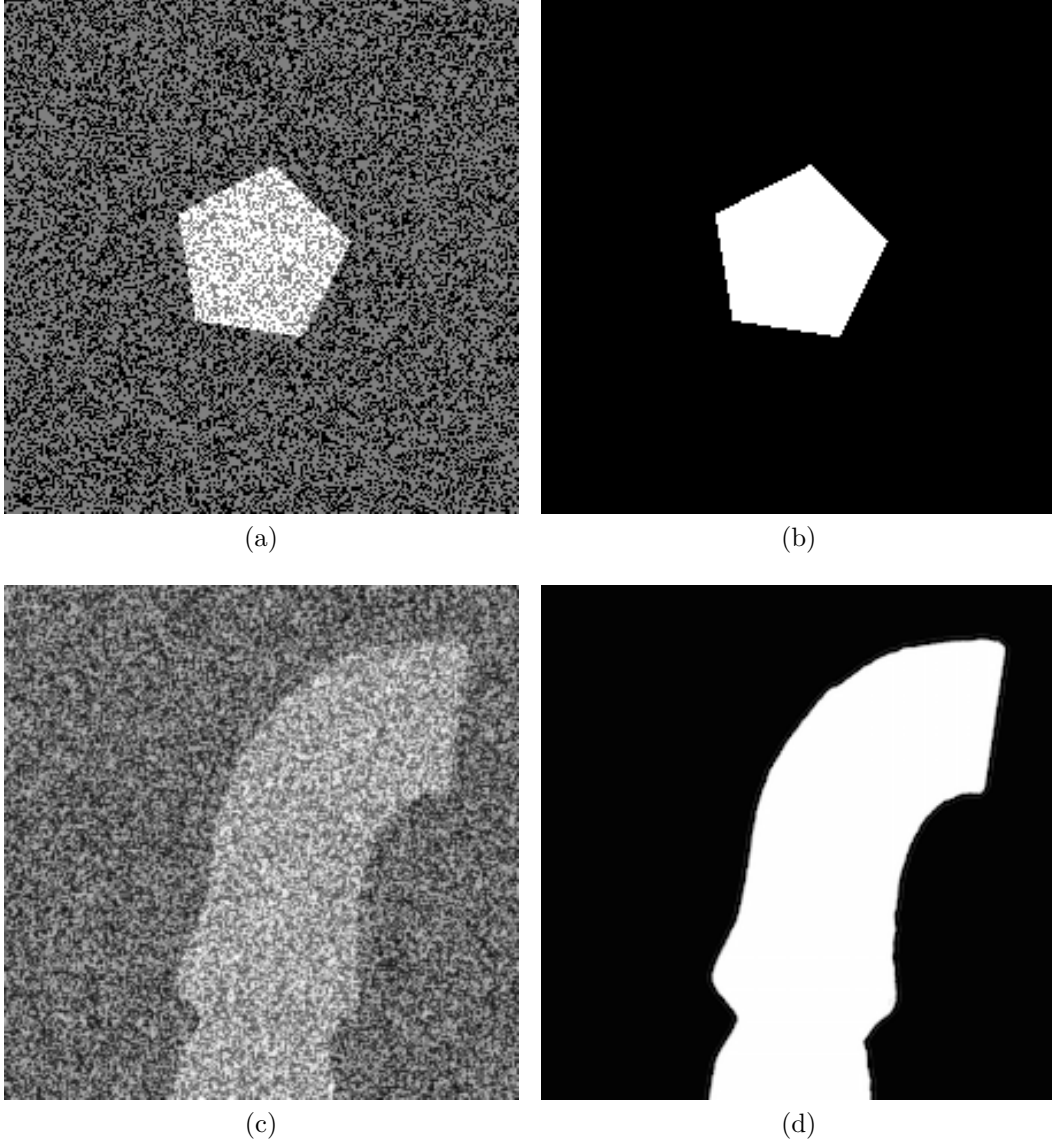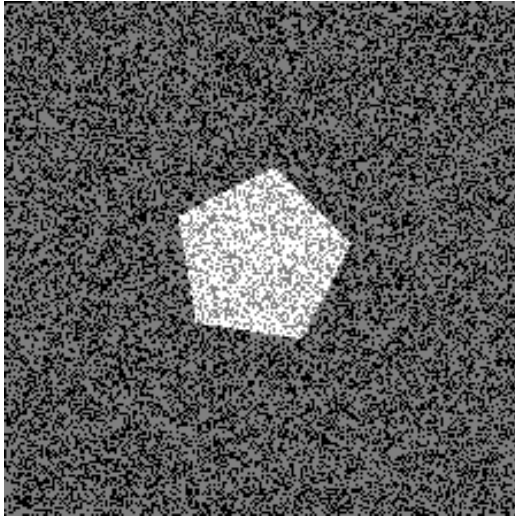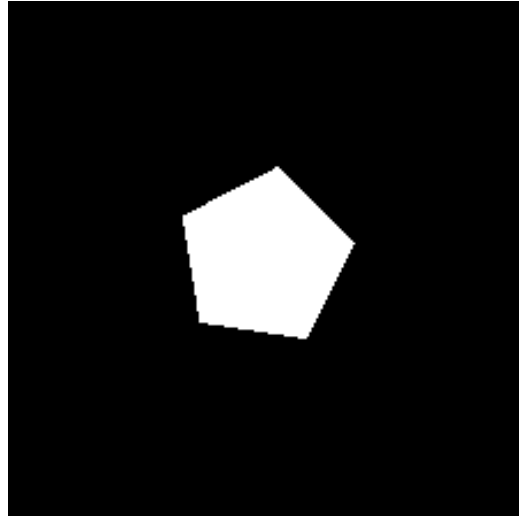
8

(a)

(b)

(c)

(d)

Figure 4: Panels (a) and (c) show examples of distorted training and validation data. Panels (b) and (d) show ground truth segmentations of the data.
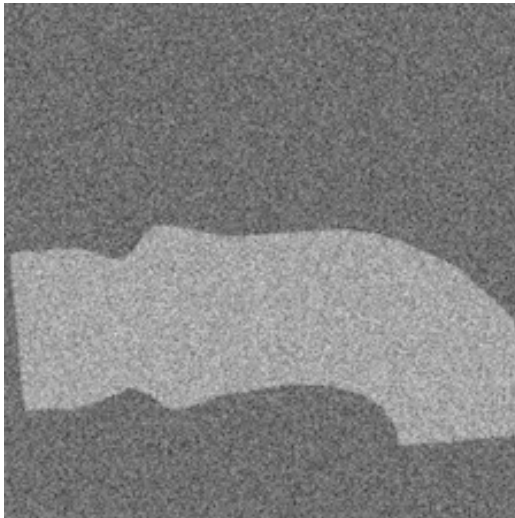
Table 3: Results with noisy shapes

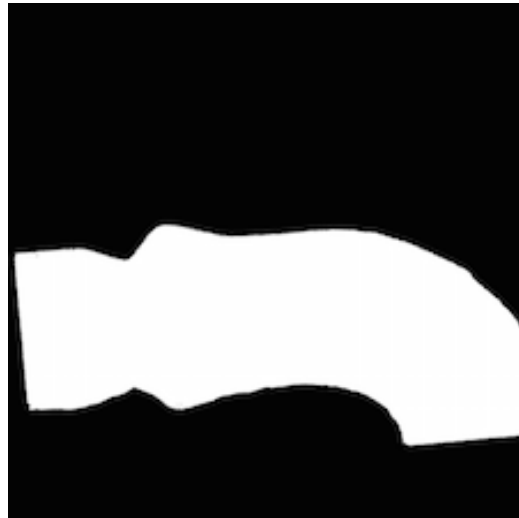| Shape	F1 Score	Avg Precision
root	97.91	98.44
pentagon	98.05	98.67

9

(a)

(b)

(c)

(d)

Figure 5: Panels (a) and (c) show examples of distorted validation data. Panels (b) and (d) show ground truth segmentations of the data. These also introduce completely new rotations unseen by the network.
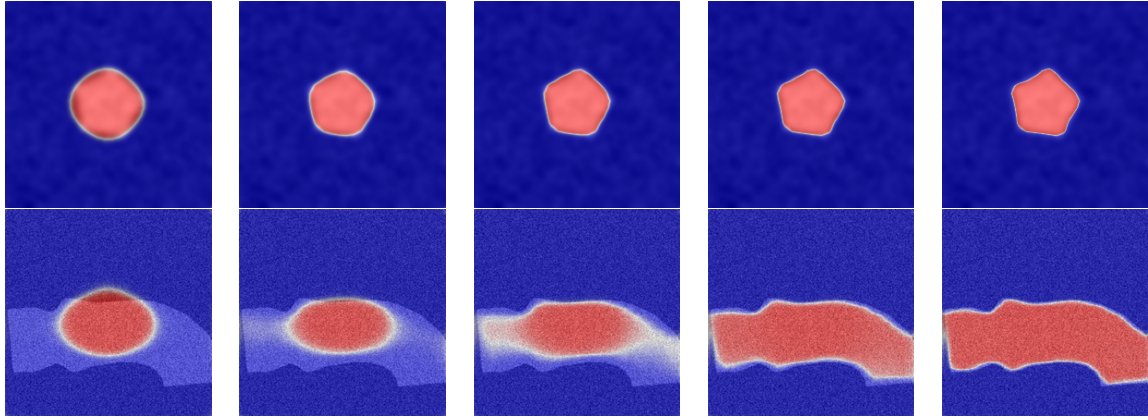
Figure 6: Evolution of validation probabilities for randomly initialized network. Each step is after 1000 iterations from the previous. Higher intensity indicates higher probability.
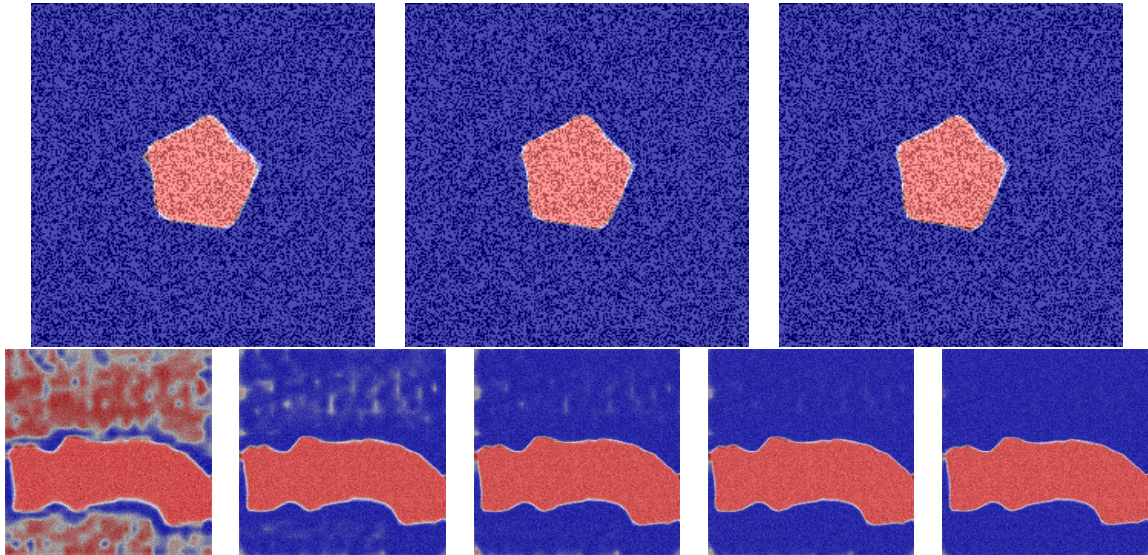

Figure 7: Evolution of validation probabilities for VGG16 initialized network. Higher intensity indicates higher probability.
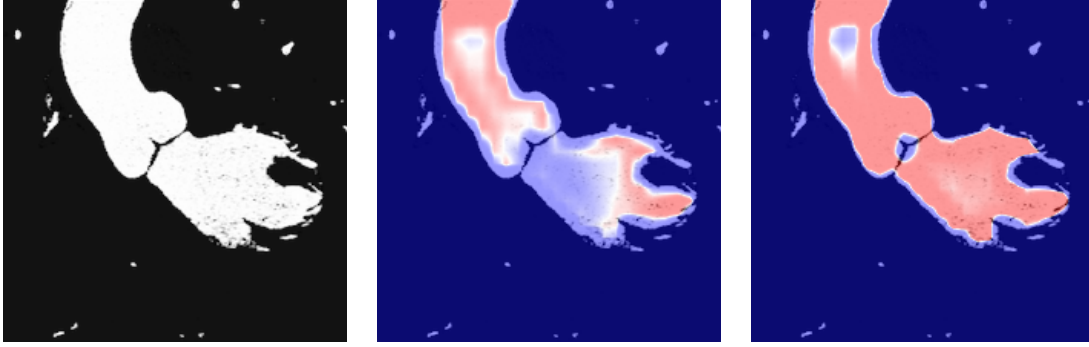
Figure 8: Evolution of validation probabilities for VGG16 initialized network tested on real data. Higher intensity indicates higher probability.

1.6   Discussion

We present two methods to enhance model construction, by using data driven methods of deforming models to generate anatomically plausible data and through an automatic method for segmentation of anatomical portions using small, easy to generate data sets. We only test the images on two dimensional images to determine the efficacy of pretrained networks. Further improvements include extension to three dimensional images and using realistic training sets. We show very promising results in the tests on synthetic data with new rotations. We also test its efficacy on realistic images. It is unclear how well this scheme applies to occluded structures, but this should also be considered. Deformation to testing data should be done to ensure global structure is achieved. A formal mathematical framework for the analysis of optimal training set size, relevant deformations, and feature selection can greatly improve modifications to the network rather than the current heuristic based modifications. Knowledge on how a particular network error may converge can be key to analyzing alterations in training or hyperparameter adjustment. Learning conditions for descriptive algorithms is another way to apply methods in deep learning in a more useful manner [18]. Finally, incorporating our generative methods into the loss function of our network to effectively generate new images that can be used to offset errors generated by the current iteration.

2   Model Simulation

The availability of open source software for fluid structure interaction vastly decreases the barriers for simulations. IBAMR [19] is an open source implementation of the

immersed boundary method. We focus on effectively simulating valve interactions.

2.1 Introduction

Heart valve replacement and repair procedures are performed with increasing frequency every year with most procedures requiring open heart surgery [20]. A minimally invasive method for valve replacement known as transcatheter aortic valve replacement (TAVR) provides a less traumatic means of valve replacement. Multiple manufacturers construct valves for use in catheters such as Medtronic's CoreValve, Edwards SAPIEN, and St. Jude Medical's PORTICO valve. Though the procedure is considerably less traumatic, constraints are imposed on the design of the valve and stent to ensure its proper functionality. Leakage in flow between the stent and the vessel wall is another common issue with TAVR [21]. It is therefore important to effectively construct and deploy valves specifically tailored to a patient's anatomy. Physics based simulation provides a platform for the development and testing of patient specific medical devices. Recent work provides descriptions of the dynamics of the aortic root with varying levels of detail.

A finite element-based fluid-structure interaction model of the aortic root was constructed using magnetic resonance imaging that accounts for geometric variability among a population of ten patients [22]. An emphasis is placed on correctly modeling the nonlinearities associated with the mechanical response of the valve leaflets. In another study, data from transesophageal echocardiography was used to construct aorta models, integrating tissue properties derived from the patient's age [23]. The model is accurately constructed by determining anatomical landmarks for Leaflet and vessel response are further tailored to the patient through the use of age dependent material properties.The efficacy of the model is assessed by comparison with patient imaging data. Finally, computational tradeoffs in numerical methods associated with such models have been examined [24]. The study discusses the necessity of including the extra computation required for fluid structure interaction in examining aortic valve motion and blood dynamics. Our model emphasizes realistic leaflet deformation and reliance on patient imaging data. We use the immersed boundary (IB) method [25] to model fluid flow through an image based aortic root to use the model as a platform for device testing and development (further discussed in section 3).
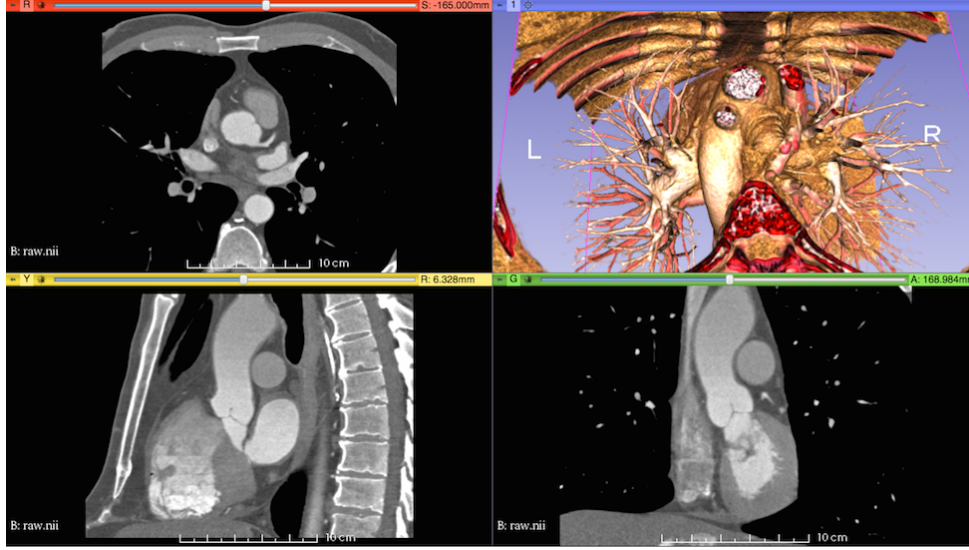
Figure 9: The computed tomography (CT) image data used in this study.

2.2 Methods

2.2.1 Model construction

A three-dimensional representation of the aortic root and ascending aorta was generated from available medical image data. This study uses one of the sample data sets from the OsiriX DICOM Image Library that consists of three-dimensional computed tomography angiography (CTA) of an anonymous patient's chest following administration of a contrast agent. The use of a contrast agent enables better discrimination of the blood vessels and heart chambers than non-contrast CT images. The image data were acquired at the Ronald Reagan University of California at Los Angeles Medical Center in Santa Monica, CA using a Siemens SOMATOM Sensation 16 CT scanner. The image resolution is 512×512×355 with a voxel size of 0.47×0.47×0.5 mm. The image was processed by an anisotropic diffusion filter to mitigate noise. Sample renderings of the patient data are shown in Fig. 9. The aortic root and ascending aorta were segmented by a semi-automated method implemented in the ITK-SNAP software.

ITK-SNAP [26, 27], which is based on the Insight Segmentation and Registration Toolkit (ITK) [28, 29], provides a graphical interface for the implementation of the active contour model, also known as Kass snakes [30], for semi-automatic segmentation. The algorithm works by minimizing an energy functional which is determined
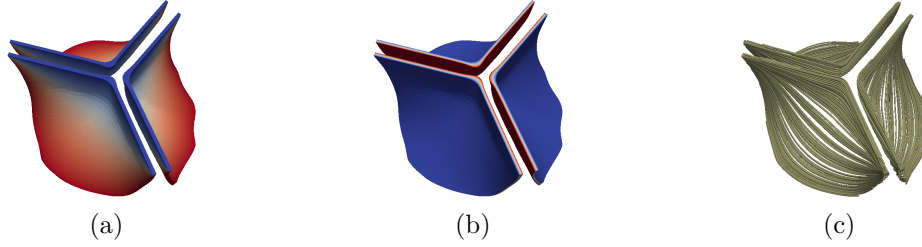
Figure 10: Idealized aortic valve leaflet geometry along with Poisson interpolation [34] based collagen fiber model. Panel (a) shows the field u that is used to define the leaflet fiber architecture, and panel (b) shows v. These fields are two solutions to the Poisson equation on the leaflet geometry, but using different boundary conditions. Panel (c) shows the resulting (mean) fiber direction, which is computed as $\mathbf{v}_1 = \nabla u \times \nabla v$. Notice that the fibers run from commissure to commissure.

by voxel intensities.

Valve leaflets are fibrous structures with multiple layers of fibers [31, 32, 33]. Modeling this fiber structure is important in describing the elasticity of the leaflets, especially when the valve is closed and is bearing a realistic pressure load. Because CTA data do not provide information about the fiber architecture of the valve leaflets, it is necessary to use a rule-based approach to describe the fiber reinforcement. To do so, we employ a method based on Poisson interpolation [34]. Briefly, we construct a local material coordinate system at each position in the leaflets by solving two Poisson problems with different sets of boundary conditions.

Multiple software packages are used to construct the full model. The construction pipeline starts with three-dimensional NRRD files containing the medical image data. Segmentation and initial geometry construction is generated using ITK-SNAP. Further adjustments are made in SOLIDWORKS (Dassault Systèmes SOLIDWORKS Corporation, Waltham, MA, USA) to fix any irregularities. SOLIDWORKS is also used to generate the geometry of the aortic valve leaflets. The derived STL from SOLIDWORKS is then used in Bolt (Computational Simulation Software, LLC, American Fork, UT, USA) to construct a hexahedral mesh for the aortic root. Placement of the model valve leaflets within the aortic root is finalized in Trelis (Computational Simulation Software, LLC, American Fork, UT, USA), which is a mesh generation software application based on CUBIT from Sandia National Laboratory.Trelis is also used to generate nonconforming hexahedral meshes of the aortic valve leaflets with approximate edge lengths of 0.75 mm. The overall model construction workflow is detailed in Fig. 11.The inflow section of the model is truncated at the left ventricular outflow tract (LVOT), and the outflow section of the model is

1. Pre-process images and establish intensity thresholds in the aortic root region.

2. Identify and apply initializing points for the semi-automated segmentation algorithm.

3. Iteratively update segmentation parameters to prevent "leaking" and to ensure propagation of the snake.

4. Export the segmentation as a STereoLithography (STL) triangulated surface mesh.

5. Import the STL geometry in CAD software to apply Gaussian smoothing and other minor modifications.

6. Export the geometry as an ACIS geometry and STL file.

7. Import the aorta geometry into Bolt for hexahedral meshing.

8. Import the geometry into Trelis for final geometry manipulation, including attachment of model valve leaflets, and valve meshing.

9. Establish boundary conditions on the valve leaflets needed for Poisson interpolation.

10. Export the mesh and boundary data as an ExodusII file for simulation.

Figure 11: Model construction workflow.

truncated in the aortic arch before the first bifurcation.

In the FSI simulation, the inflow and outflow sections are coupled to reduced-order models that provide driving and loading conditions, and that establish realistic pressure differences across the model vessel.

2.2.2 Immersed boundary method

We use the IB method with fluid momentum conservation and incompressibility equations are formulated on a fixed Eularian domain $\Omega \subset \mathbb{R}^3$ and solid mechanics formulations on a Lagrangian coordinate system. The domain is divided into fluid and solid parts where $\Omega = \Omega^{\mathrm{f}}(t) \cup \Omega^{\mathrm{s}}(t)$ and $\Omega^{\mathrm{f}} \cap \Omega^{\mathrm{s}} = \emptyset$. We define reference coordinates $s = (X_1, X_2, X_3) \in U \subset \mathbb{R}^3$ and a mapping $\boldsymbol{\chi}(\mathbf{X}, t)$ relating reference to physical coordinates. Then $\Omega^{\mathrm{s}}(t) \equiv \boldsymbol{\chi}(U, t)$. We use the 1st Piola-Kirchhoff stress tensor relating reference coordinates to stress. We write the fluid solid interaction
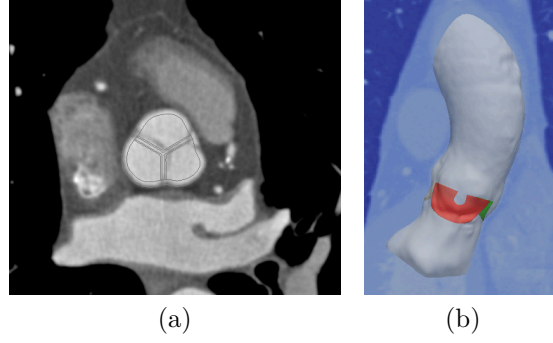
(a)   (b)

Figure 12: Panels (a) two-dimensional projection of leaflet alignment between model and image, axial view; and (b) three-dimensional model fit with original data, sagittal view.

equations in the following manner:

$$\rho \frac{\mathrm{D}\mathbf{u}}{\mathrm{D}t}(\mathbf{x}, t) = -\nabla p(\mathbf{x}, t) + \mu \nabla^2 \mathbf{u}(\mathbf{x}, t) + \mathbf{f}(\mathbf{x}, t) + \mathbf{t}(\mathbf{x}, t), \tag{7}$$

$$\nabla \cdot \mathbf{u}(\mathbf{x}, t) = 0, \tag{8}$$

$$\mathbf{f}(\mathbf{x}, t) = \int_U \mathbf{F}(\mathbf{X}, t)\, \delta(\mathbf{x} - \boldsymbol{\chi}(\mathbf{X}, t))\, \mathrm{d}\mathbf{X}$$

$$+ \int_U \nabla \cdot \mathbb{P}^{\mathrm{s}}(\mathbf{X}, t)\, \delta(\mathbf{x} - \boldsymbol{\chi}(\mathbf{X}, t))\, \mathrm{d}\mathbf{X}, \tag{9}$$

$$\mathbf{t}(\mathbf{x}, t) = -\int_{\partial U} \mathbb{P}^{\mathrm{s}}(\mathbf{X}, t)\, \mathbf{N}(\mathbf{X})\, \delta(\mathbf{x} - \boldsymbol{\chi}(\mathbf{X}, t))\, \mathrm{d}A, \tag{10}$$

$$\mathbb{P}^{\mathrm{s}}(\mathbf{X}, t) = J\, \boldsymbol{\sigma}^{\mathrm{s}}(\mathbf{X}, t)\, \mathbb{F}^{-T}, \tag{11}$$

$$\frac{\partial \boldsymbol{\chi}}{\partial t}(\mathbf{X}, t) = \int_\Omega \mathbf{u}(\mathbf{x}, t)\, \delta(\mathbf{x} - \boldsymbol{\chi}(\mathbf{X}, t))\, \mathrm{d}\mathbf{x} = \mathbf{u}(\boldsymbol{\chi}(\mathbf{X}, t), t), \tag{12}$$

The solid and fluid move at the same velocity $u(\mathbf{x}, t)$ at the fluid structure boundaries leading to a continuous velocity field. $u(\mathbf{x}, t)$ is the velocity field, $p(\mathbf{x}, t)$ is the pressure field, μ is the viscosity, ρ is the mass density, $\delta(\mathbf{x}) = \Pi_{i=1}^3 \delta x_i$ is the 3-dimensional Dirac-delta function, $\frac{\mathrm{D}\mathbf{u}}{\mathrm{D}t}$ is the material derivative, $\mathbf{f}$ denotes body forces and $\mathbf{t}$ denotes surface forces.

2.2.3   Solid mechanics model

We model the solid as a nearly incompressible solid with different models for the vessel wall and the leaflets. Both materials are modeled with a hyperelastic material

17

response, with the first Piola-Kirchhoff stress tensor modeled as $\mathbb{P}^{\mathrm{s}} = \frac{\partial \bar{W}}{\partial \mathbb{F}}$. The strain energy is then assumed to be partitioned additively into isochoric and volumetric parts, $W(\mathbb{F}) = \bar{W}(\bar{\mathbb{F}}) + U(J)$. The isotropic matrix is described by:

$$\bar{W}_{\mathrm{matrix}} = \frac{c_1}{2}(\bar{I}_1 - 1), \tag{13}$$

The elastic fibers are described by:

$$\bar{W}_{\mathrm{f},i} = \frac{k_1}{2k_2} \left(\exp \left(k_2(\bar{I}^\star_{4\mathrm{f},i} - 1) \right) - k_2 \bar{I}^\star_{4\mathrm{f},i} \right), \tag{14}$$

in which i indexes a discrete collection of fiber directions, $\mathbf{e}^0_{\mathrm{f},i}$ is a unit vector in the ith fiber direction in the reference configuration, $\bar{I}_{4\mathrm{f},i}$ is the fiber invariant,

$$\bar{I}_{4\mathrm{f},i} = \mathbf{e}^0_{\mathrm{f},i} \cdot \bar{\mathbb{C}} \, \mathbf{e}^0_{\mathrm{f},i}, \tag{15}$$

and $\bar{I}^\star_{4\mathrm{f},i}$ is the modified fiber invariant,

$$\bar{I}^\star_{4\mathrm{f},i} = \begin{cases} \bar{I}_{4\mathrm{f},i} & \text{if } \bar{I}_{4\mathrm{f},i} \geq 1, \\ 0 & \text{otherwise.} \end{cases} \tag{16}$$

We use $c_1 = 10$ kPa, $k_1 = 0.7$ kPa, and $k_2 = 9.9$, which corresponds to material properties of fresh porcine heart valve leaflets determined by experimental studies of Billiar and Sacks [35, 36].

The fiber reinforced model of Driessen, Bouten, and Baaijens [33] describes a neo-Hookean description of the leaflet matrix

The vessel wall is modeled as a stiff neo-Hookean material where $\bar{W} = \frac{c}{2}(I_1 - 3)$ with body forces $\mathbf{F}(\mathbf{X}, t) = \kappa^{\mathrm{s}} (\mathbf{X} - \boldsymbol{\chi}(\mathbf{X}, t))$ providing additional structural forces to keep the vessel held in place.

2.2.4 Boundary conditions

We adjust the vessel geometry to fit a rectangular domain where we impose boundary conditions at the inlets and outlets. Let $\partial\Omega_{\mathrm{in}}$ and $\partial\Omega_{\mathrm{out}}$ indicate the inlet and outlet boundaries of the domain, and let P_{in} and Q_{in} (respectively, P_{out} and Q_{out}) indicate the mean pressure and net flow rate along the inlet (respectively, outlet) boundary. Inflow is reconciled by a linear resistance model where

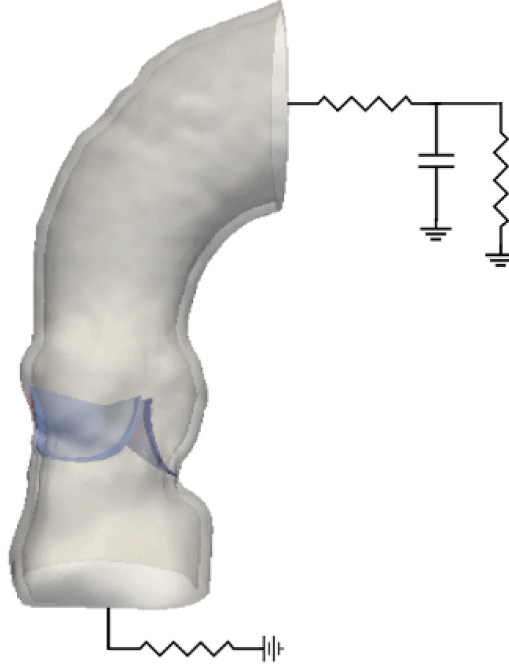$$(P_{\mathrm{LV}} - P_{\mathrm{in}}) = R_{\mathrm{src}} Q_{\mathrm{in}}, \tag{17}$$

Figure 13: Boundary condition circuit analogue.

where $R_{\mathrm{src}} = 0.05$ mmHg/(ml/s) and $P_{\mathrm{LV}}(t)$ is determined from the "Type A" clinical pressure and flow rates collected by Murgo et al. [37]. At the outlet, we reconcile the model to the three-element Windkessel model of Stergiopulos et al. [38], using "Type A" parameters fit using the Levenberg-Marquardt algorithm to clinical pressure and flow rates collected by Murgo et al. [37].

2.2.5 Numerical methods

We use finite difference scheme for the fluid solve and finite element scheme for the solid coupling based on the methods discussed by Griffith and Luo [39] with a standard selective reduced integration method [40] to treat penalty terms in the leaflets. We use hexahedral first order Q^1 elements for the vessel and second order P^2 elements for the leaflets. A three-point delta function introduced by Roma et al. [41] is used for the vessel wall, and a six point "Gaussian-like" kernel for the leaflets to reduce leakage described by Bao, Kaye, and Peskin [42].
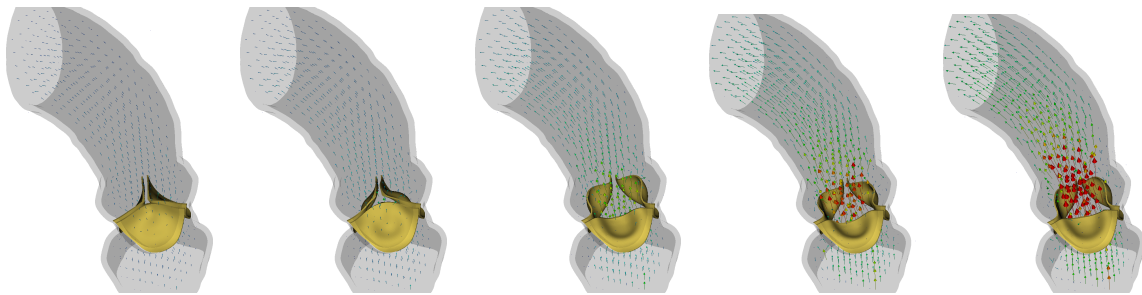
19

Figure 14: Valve opening dynamics, showing the leaflet kinematics and fluid dynamics. Peak flow velocities during early systole, highlighted in red, are approximately 2 m/s.

2.3 Results

Figures 14, 15, and 16 provide the resulting dynamics of the system. The model is driven as described previously using left ventricular pressure waveform [37], and outlet provided by a three-element Windkessel model fit to those same data [38]. In our simulations, we use a fluid viscosity of 4 cP and mass density of 1 g/cm^3, and we set the computational domain Ω to be a 5.5 cm $\times$ 5.5 cm $\times$ 11 cm box that is discretized using an adaptively refined Cartesian grid with an effective resolution of 0.86 mm. We use a fixed time step size $\Delta t = 2.5 \times 10^{-5}$ s, which is required by stability constraints imposed both by our explicit coupling between the Eulerian and Lagrangian variables.

2.4 Discussion

We describe the methods used to create a patient specific model using the IB method. The model uses clinical imaging along with a realistic description of valve fibers. However, the model has many portions for further analysis. Realistic deformations of the root geometry based on appropriate material parameters is a necessary next step. By finding material parameters that lead to a proper deformation of the vessel wall from its resting configuration, we can accurately find the elastic properties of the vessel. Determining the effects of bicuspid or quadricuspid valves on a geometry can also be studied. The modularity of the model lends itself to be easily extensible. Studying the effects of calcification of valve leaflets or narrowing of the aorta on blood flow are further avenues to extend this study. Such complications are common in a variety of cardiac related diseases.
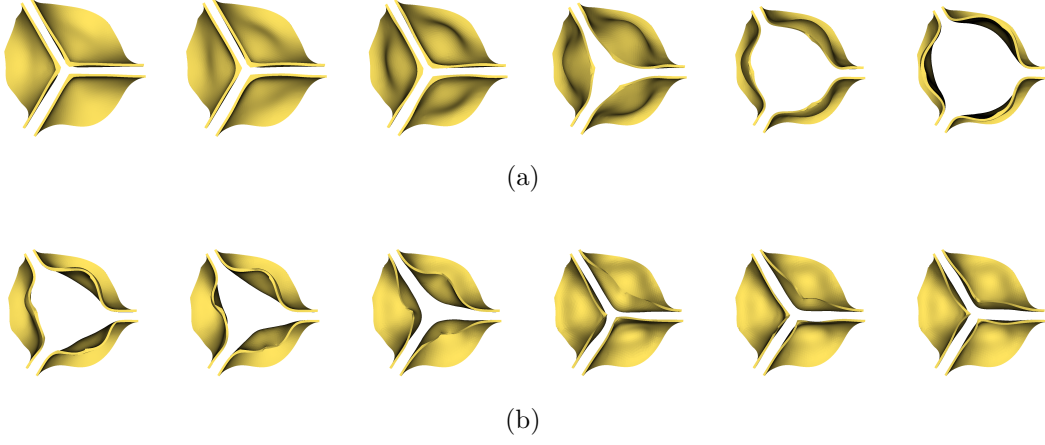
(a)

(b)

Figure 15: Valve kinematics during (a) opening and (b) closure, shown at equally spaced intervals. The gap between the closed valve leaflets reflects the thickness of the regularized delta function. Despite this residual gap, the valve is sealed with respect to the fluid, as demonstrated in Fig. 16, which shows that the closed valve supports a physiological pressure load without leak.
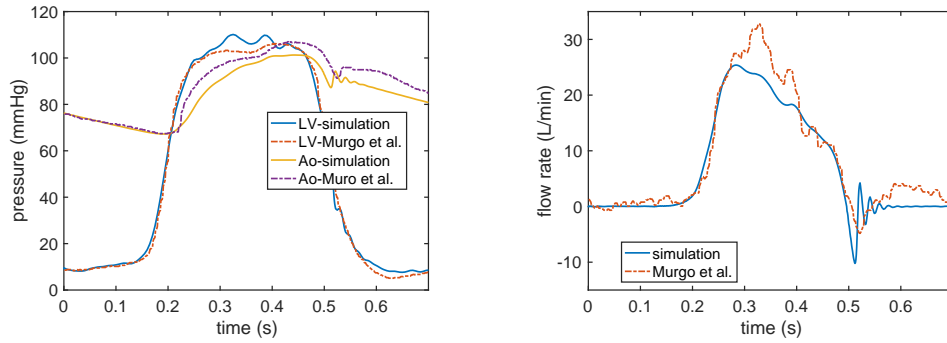

Figure 16: A comparison of our generated and clinical (ground truth) left ventricular and aortic pressures (left) and flow rates (right).

Acknowledgements

References

[1] M. Kass, A. Witkin, and D. Terzopoulos, "Snakes: Active contour models," *International journal of computer vision*, vol. 1, no. 4, pp. 321–331, 1988.

[2] S. Osher and J. A. Sethian, "Fronts propagating with curvature-dependent speed: algorithms based on hamilton-jacobi formulations," *Journal of computational physics*, vol. 79, no. 1, pp. 12–49, 1988.

[3] D. Cremers, F. R. Schmidt, and F. Barthel, "Shape priors in variational image segmentation: Convexity, lipschitz continuity and globally optimal solutions," in *Computer Vision and Pattern Recognition, 2008. CVPR 2008. IEEE Conference on*, pp. 1–6, IEEE, 2008.

[4] A. Tsai, A. Yezzi, W. Wells, C. Tempany, D. Tucker, A. Fan, W. E. Grimson, and A. Willsky, "Model-based curve evolution technique for image segmentation," in *Computer Vision and Pattern Recognition, 2001. CVPR 2001. Proceedings of the 2001 IEEE Computer Society Conference on*, vol. 1, pp. I–I, IEEE, 2001.

[5] T. F. Cootes, C. J. Taylor, D. H. Cooper, and J. Graham, "Active shape models-their training and application," *Computer vision and image understanding*, vol. 61, no. 1, pp. 38–59, 1995.

[6] J. Long, E. Shelhamer, and T. Darrell, "Fully convolutional networks for semantic segmentation," in *Proceedings of the IEEE Conference on Computer Vision and Pattern Recognition*, pp. 3431–3440, 2015.

[7] F. Milletari, N. Navab, and S.-A. Ahmadi, "V-net: Fully convolutional neural networks for volumetric medical image segmentation," in *3D Vision (3DV), 2016 Fourth International Conference on*, pp. 565–571, IEEE, 2016.

[8] T. Zhou, S. Tulsiani, W. Sun, J. Malik, and A. A. Efros, "View synthesis by appearance flow," in *European Conference on Computer Vision*, pp. 286–301, Springer, 2016.

[9] D. Nie, R. Trullo, C. Petitjean, S. Ruan, and D. Shen, "Medical image synthesis with context-aware generative adversarial networks," *arXiv preprint arXiv:1612.05362*, 2016.

[10] I. Goodfellow, J. Pouget-Abadie, M. Mirza, B. Xu, D. Warde-Farley, S. Ozair, A. Courville, and Y. Bengio, "Generative adversarial nets," in *Advances in neural information processing systems*, pp. 2672–2680, 2014.

[11] J. Z. Chen, S. M. Pizer, E. L. Chaney, and S. Joshi, "Medical image synthesis via monte carlo simulation," in *International Conference on Medical Image Computing and Computer-Assisted Intervention*, pp. 347–354, Springer, 2002.

[12] K. Simonyan and A. Zisserman, "Very deep convolutional networks for large-scale image recognition," *arXiv preprint arXiv:1409.1556*, 2014.

[13] O. Russakovsky, J. Deng, H. Su, J. Krause, S. Satheesh, S. Ma, Z. Huang, A. Karpathy, A. Khosla, M. Bernstein, *et al.*, "Imagenet large scale visual recognition challenge," *International Journal of Computer Vision*, vol. 115, no. 3, pp. 211–252, 2015.

[14] M. Teichmann, M. Weber, M. Zoellner, R. Cipolla, and R. Urtasun, "Multinet: Real-time joint semantic reasoning for autonomous driving," *arXiv preprint arXiv:1612.07695*, 2016.

[15] C. E. Shannon, "A mathematical theory of communication," *ACM SIGMOBILE Mobile Computing and Communications Review*, vol. 5, no. 1, pp. 3–55, 2001.

[16] D. Kingma and J. Ba, "Adam: A method for stochastic optimization," *arXiv preprint arXiv:1412.6980*, 2014.

[17] M. Abadi, A. Agarwal, P. Barham, E. Brevdo, Z. Chen, C. Citro, G. S. Corrado, A. Davis, J. Dean, M. Devin, *et al.*, "Tensorflow: Large-scale machine learning on heterogeneous distributed systems," *arXiv preprint arXiv:1603.04467*, 2016.

[18] X. Yang, R. Kwitt, and M. Niethammer, "Fast predictive image registration," in *International Workshop on Large-Scale Annotation of Biomedical Data and Expert Label Synthesis*, pp. 48–57, Springer, 2016.

[19] B. Griffith, "Ibamr: An adaptive and distributed-memory parallel implementation of the immersed boundary method."

[20] A. P. Yoganathan, Z. He, and S. Casey Jones, "Fluid mechanics of heart valves," *Annu. Rev. Biomed. Eng.*, vol. 6, pp. 331–362, 2004.

[21] J.-B. Masson, J. Kovac, G. Schuler, J. Ye, A. Cheung, S. Kapadia, M. E. Tuzcu, S. Kodali, M. B. Leon, and J. G. Webb, "Transcatheter aortic valve implantation review of the nature, management, and avoidance of procedural complications," *JACC Cardiovasc Interv*, vol. 2, no. 9, pp. 811–820, 2009.

[22] C. A. Conti, E. Votta, A. Della Corte, L. Del Viscovo, C. Bancone, M. Cotrufo, and A. Redaelli, "Dynamic finite element analysis of the aortic root from MRI-derived parameters," *Med Eng Phys*, vol. 32, no. 2, pp. 212–221, 2010.

[23] M. R. Labrosse, C. J. Beller, M. Boodhwani, C. Hudson, and B. Sohmer, "Subject-specific finite-element modeling of normal aortic valve biomechanics from 3d+ t tee images," *Med Image Anal*, vol. 20, no. 1, pp. 162–172, 2015.

[24] F. Sturla, E. Votta, M. Stevanella, C. A. Conti, and A. Redaelli, "Impact of modeling fluid-structure interaction in the computational analysis of aortic root biomechanics," *Med Eng Phys*, vol. 35, no. 12, pp. 1721–1730, 2013.

[25] C. S. Peskin, "The immersed boundary method," *Acta numerica*, vol. 11, pp. 479–517, 2002.

[26] P. A. Yushkevich, J. Piven, H. Cody Hazlett, R. Gimpel Smith, S. Ho, J. C. Gee, and G. Gerig, "User-guided 3D active contour segmentation of anatomical structures: Significantly improved efficiency and reliability," *Neuroimage*, vol. 31, no. 3, pp. 1116–1128, 2006.

[27] "ITK-SNAP." http://www.itksnap.org.

[28] H. J. Johnson, M. McCormick, L. Ibáñez, and The Insight Software Consortium, "The ITK Software Guide," 2015.

[29] "The Insight Segmentation and Registration Toolkit." http://www.itk.org.

[30] M. Kass, A. Witkin, and D. Terzopoulos, "Snakes: Active contour models," *Int J Comput Vision*, vol. 1, no. 4, pp. 321–331, 1988.

[31] A. F. Sauren, *The mechanical behaviour of the aortic valve.* PhD thesis, Technische Hogeschool Eindhoven, 1981.

[32] J. De Hart, G. Peters, P. Schreurs, and F. Baaijens, "Fluid-structure interaction in the aortic heart valve: a three-dimensional computational analysis," 2002.

[33] N. J. B. Driessen, C. V. C. Bouten, and F. P. T. Baaijens, "A structural constitutive model for collagenous cardiovascular tissues incorporating the angular fiber distribution," *J Biomech Eng*, vol. 127, no. 3, pp. 494–503, 2005.

[34] J. Wong and E. Kuhl, "Generating fibre orientation maps in human heart models using poisson interpolation," *Comput Methods Biomech Biomed Engin*, vol. 17, no. 11, pp. 1217–1226, 2014.

[35] K. L. Billiar and M. S. Sacks, "Biaxial mechanical properties of the natural and glutaraldehyde treated aortic valve cusp. Part I: Experimental results," *J Biomech Eng*, vol. 122, no. 1, pp. 23–30, 2000.

[36] K. L. Billiar and M. S. Sacks, "Biaxial mechanical properties of the native and glutaraldehyde-treated aortic valve cusp. Part II: A structural constitutive model," *J Biomech Eng*, vol. 122, no. 4, pp. 327–335, 2000.

[37] J. P. Murgo, N. Westerhof, J. P. Giolma, and S. A. Altobelli, "Aortic input impedance in normal man: relationship to pressure wave forms," *Circulation*, vol. 62, no. 1, pp. 105–116, 1980.

[38] N. Stergiopulos, B. E. Westerhof, and N. Westerhof, "Total arterial inertance as the fourth element of the windkessel model," *American Journal of Physiology-Heart and Circulatory Physiology*, vol. 276, no. 1, pp. H81–H88, 1999.

[39] B. E. Griffith and X. Luo, "Hybrid finite difference/finite element immersed boundary method," *arXiv preprint arXiv:1612.05916*, 2016.

[40] T. Belytschko, W. K. Liu, B. Moran, and K. Elkhodary, *Nonlinear finite elements for continua and structures*. John wiley & sons, 2013.

[41] A. M. Roma, C. S. Peskin, and M. J. Berger, "An adaptive version of the immersed boundary method," *Journal of computational physics*, vol. 153, no. 2, pp. 509–534, 1999.

[42] Y. Bao, J. Kaye, and C. S. Peskin, "A gaussian-like immersed boundary kernel with three continuous derivatives and improved translational invariance." arXiv:1505.07529 [math.NA], 2015.